Materials Advances

ROYAL SOCIETY OF CHEMISTRY

PAPER

View Article Online
View Journal | View Issue

Cite this: *Mater. Adv.*, 2025, 6, 2899

Polymer-derived N-doped carbon nanomaterials containing carbon nano-onions and their potential applicability†

Agnieszka Hryniewicka, *[a] Joanna Breczko,[b] Gabriela Siemiaszko,[a] Karolina H. Markiewicz,[b] Agnieszka Gabryelczyk,[c] Grzegorz Lota[cd] and Marta E. Plonska-Brzezinska *[a]

Received 15th December 2024,
Accepted 16th March 2025

DOI: 10.1039/d4ma01230e

rsc.li/materials-advances

Herein, we report the synthesis and characterization of materials consisting of carbon nano-onions (CNOs) and N and S atom-containing polymer precursors, readily available from polyacrylonitrile(**PAN**)–poly(acrylic esters) block copolymers. Two different acrylic esters were used, methyl and butyl acrylate carbon chains that formed a polymeric network with varying pore sizes on the CNO's surface. Their material counterparts without CNOs were also synthesized as reference materials. The polymers were annealed in airflow to stabilize **PAN** domains, followed by pyrolysis at 800 °C under an argon atmosphere. The N-rich carbon nanomaterials were loaded with S in the mixing–melting–diffusion process, resulting in S loading at 51–57 wt%. The synthesized N-doped carbon materials were used as positive electrodes in Li–S batteries. The battery with the CNO-based nanomaterial provided over 20% higher capacity than that without CNO. This suggests that designing and preparing N-doped carbon nanomaterials containing CNOs could be a promising direction in the search for cathode materials in Li–S batteries.

Introduction

Heteroatom-doped porous carbon materials possess unique features, such as high surface area, excellent mechanical properties, and good thermal stabilities.[1,2] N-doped porous carbon materials are extensively investigated due to their promising electrochemical properties. They have been widely used in energy storage and conversion (*e.g.*, supercapacitors[3–5] and batteries[6]), electrocatalysis (*e.g.*, oxygen reduction reaction[7]), and others (*e.g.*, capacitive deionization[8]).[9–12] Heteroatom doping can be realized by two strategies: post-treatment or *in situ* methods. A post-treatment doping strategy is usually applied for heteroatom incorporation into final carbon materials, *e.g.*, sulfur can be loaded by heating the mixture of S_8 and carbon at about 155 °C under an inert gas.[13] The *in situ* doping approach introduces heteroatoms by utilizing heteroatom-containing carbon precursors.[14] A facile method for obtaining N-rich polymer-derived carbon materials is the thermal treatment of polyacrylonitrile (**PAN**)[2] due to its ability to cyclize and cross-link to form fused aromatic rings by condensation of ladder structures.[15]

In practice, the **PAN** pyrolysis method is used to obtain N-doped carbon materials and primarily to synthesize highly porous carbon nanomaterials (CNMs). It is possible thanks to the use of a copolymer consisting of **PAN** (as a carbon matrix) and a thermodegradable sacrificial block (usually poly(acrylic ester), *e.g.*, poly(methyl methacrylate) – PMMA).[16] Its pyrolysis leads to the formation of partially graphitic carbon from **PAN** and the removal of sacrificial ester blocks with the simultaneous generation of porosity.[17] Using block copolymers as templates has proven to be an effective method for obtaining CNMs suitable for energy storage applications.[18,19]

Achieving hierarchical porosity comprising micro- and mesopores is essential for electrical double-layer formation and improved ion accessibility and diffusion.[20] Block copolymers are usually obtained by controlled radical polymerization,

[a] *Department of Organic Chemistry, Faculty of Medicine with the Division of Dentistry and Division of Medical Education In English, Medical University of Bialystok, Mickiewicza 2A, 15-222 Bialystok, Poland. E-mail: agnieszka.hryniewicka@umb.edu.pl, marta.plonska-brzezinska@umb.edu.pl*

[b] *Faculty of Chemistry, University of Bialystok, Ciolkowskiego 1K, 15-245 Bialystok, Poland*

[c] *Faculty of Chemical Technology, Institute of Chemistry and Technical Electrochemistry, Poznan University of Technology, Berdychowo 4, 60-965 Poznan, Poland*

[d] *Łukasiewicz Research Network – Institute of Non-Ferrous Metals Division in Poznan, Central Laboratory of Batteries and Cells, Forteczna 12, 61-362 Poznan, Poland*

† Electronic supplementary information (ESI) available. See DOI: https://doi.org/10.1039/d4ma01230e

which affords functional polymers with a predefined length, composition, dispersity, and end groups. Reversible addition-fragmentation chain-transfer (RAFT) and atom transfer radical polymerizations (ATRP) are the two most common methods of controlled radical polymerization that help in designing well-defined, functional materials for a broad range of applications.[21] RAFT polymerization facilitates more control over the polymerization process, such as a predefined and narrow range of molecular weights. This user-friendly method can be applied to various monomer families with different side-chain functionalities.[22]

Carbon–sulfur composites are often applied as the cathode of rechargeable Li–S batteries due to their outstanding electrochemical performance for high-power devices. Li–S batteries are among the most promising next-generation batteries due to their ultra-high theoretical specific capacity and energy density, as well as the easy availability and price of sulfur. Their electrochemical performance is still being improved thanks to numerous studies on sulfur composite cathodes[23] containing, *e.g.*, graphene,[24] carbon nanotubes,[25] or carbon nano-onions (CNOs).[26] However, despite continued interest over the years, Li–S batteries have some limitations, such as poor cycling stability due to polysulfide shuttling and reduced charging rate, and power density due to the low electrical conductivity of sulfur.[27]

CNOs, also called multilayered fullerenes, are nanoparticles with a 4–25 nm diameter, consisting of concentric shells of graphitic carbon.[28] They have attracted significant attention due to their structural and physicochemical properties. This, in turn, made it possible to use them in many areas, such as electronics,[29] optics,[30] energy conversion and storage devices.[31,32] Presser *et al.* obtained a composite of sulfur and CNO, which was found to be an efficient cathode for Li–S batteries, yielding 97–98% coulombic efficiency over 150 cycles with a slow fading of the specific capacity in a long-term cycle test and rate capability experiments.[26] Zhang *et al.* reported a carbon **PAN**–PMMA-derived nanofiber sulfur composite as an electrode for Li–S batteries. Although the porosity of the fiber is moderate, the electrodes maintain a stable discharge capacity of about 1400 mA h g^{-1} at 0.05C.[33] Recently, we proved that introducing only a tiny amount of CNOs, approximately 5 wt%, improved the electrochemical properties of carbon materials.[34–38]

Herein, we propose to use N-doped CNM with loaded S (**CNO–CNM-S**) as the electrode material in Li–S batteries, readily available from block **PAN**–poly(acrylic ester) copolymers after thermal treatment and heating with sulfur. This approach uses only a tiny amount of CNOs (3 wt%).[39] Moreover, the 'pristine' carbon nanomaterial (**CNM-S**) obtained analogically but without CNOs will be used as a reference material. Thanks to this, it will be possible to precisely determine the influence of CNOs on the properties of the synthesized materials.

Results and discussion

Synthesis

CNO–CNM-S derived from well-defined copolymers arranged on CNOs were synthesized using the RAFT polymerization method, subsequent thermal treatment and sulfur loading (Fig. 1). Their counterparts without CNOs (**CNM-S**) were also synthesized for comparison with hybrids. To provide covalent linking between CNOs and CNMs, carbon nanoparticles were functionalized with 1-azido-4-(methyl)benzyl dithiobenzoate (**CTA-N_3**) as it can act as a carbon-supported chain transfer agent. The reaction between CNOs and **CTA-N_3**, giving **f-CNO**, was carried out in dichlorobenzene (DCB) at reflux, resulting in the formation of an aziridine ring with the C=C group on the CNO surface (Fig. 1). Thermogravimetric analysis (TGA) of **f-CNO** showed an 11% weight loss in the range of 200–600 °C confirming the modification of the carbon nanostructure (Fig. S12, ESI†). Then, **f-CNO** was subjected to a controlled reaction with acrylonitrile (AN). The polymeric chain of **PAN** contains approximately 220 units based on nuclear magnetic resonance spectroscopic (^{1}H NMR) studies (Fig. S4 and Table S1, ESI†). It was calculated from doublet at about 8.05 ppm derived from 2 protons of CTA. By comparison of the integration of the CTA moiety and signal from the C*H*(CN) group in the polymer chain at 3.18 ppm, we were able to calculate the number of AN units in **CNO-PAN** (220 AN units, Table S4, ESI†). The polymer was subsequently subjected to a reaction with methyl acrylate (MA) or butyl acrylate (BA) to give **CNO-PAN–PMA** and **CNO-PAN–PBA** copolymers, respectively (Tables S2 and S4, ESI†). The mass fraction of **PMA** chains (wt% **PMA**) in **CNO-PAN–PMA** was determined based on the integration of the $-CH_3$ signal of ester groups and the proton adjacent to nitrile (–C*H*CN) in the ^{1}H NMR spectra, providing a value of 57%; the number of MA units was estimated to be 180 (Fig. S8, ESI†). The mass fraction of PBA chains (wt% PBA) in **CNO-PAN–PBA** was 58%, and the number of BA units was estimated to be 126, according to the integration of the $-CH_2$ signal of ester groups and the proton adjacent to the nitrile (–C*H*CN) (Fig. S9, ESI†). Similarly, as described above for **CNO-PAN**, AN was subjected to a reaction with CTA to form **PAN** with a predefined length as the first block. The repeating unit of polymer consisting of AN moieties was estimated theoretically to be 200 units. According to ^{1}H NMR, the number of AN units was 186, constituting 93% of the estimated amount (Fig. S7, ESI†). It was calculated in the same manner as **CNO-PAN**. Polymer **PAN** was subsequently subjected to a reaction with MA or BA to give **PAN–PMA** and **PAN–PBA** copolymers, respectively. Based on ^{1}H NMR spectra, the number of MA units was 123 (200 assumed), and BA was 137 (200 assumed) (Table S3, ESI†), which consisted of 52% of **PMA** in **PAN–PMA** and 64% of PBA in **PAN–PBA** (Fig. S5, S6 and Table S5, ESI†), respectively.

The polymers with and without CNOs were then subjected to annealing for 1 h at 280 °C under airflow to stabilize **PAN** domains and then pyrolyzed for 30 minutes at 800 °C under an argon atmosphere to remove the sacrificial block. Four **CNM-1**, **CNM-2**, **CNO–CNM-1**, and **CNO–CNM-2** materials were obtained as the black solids. During thermal treatment, the samples' weight loss (57–66%) indicated pores forming in the carbon structures (Table S5, ESI†). The CNO content was *ca.* 3% in the **CNO–CNM-1** and **CNO–CNM-2** materials (Table S5, ESI†). This amount was chosen based on our previous investigation.[34–38]

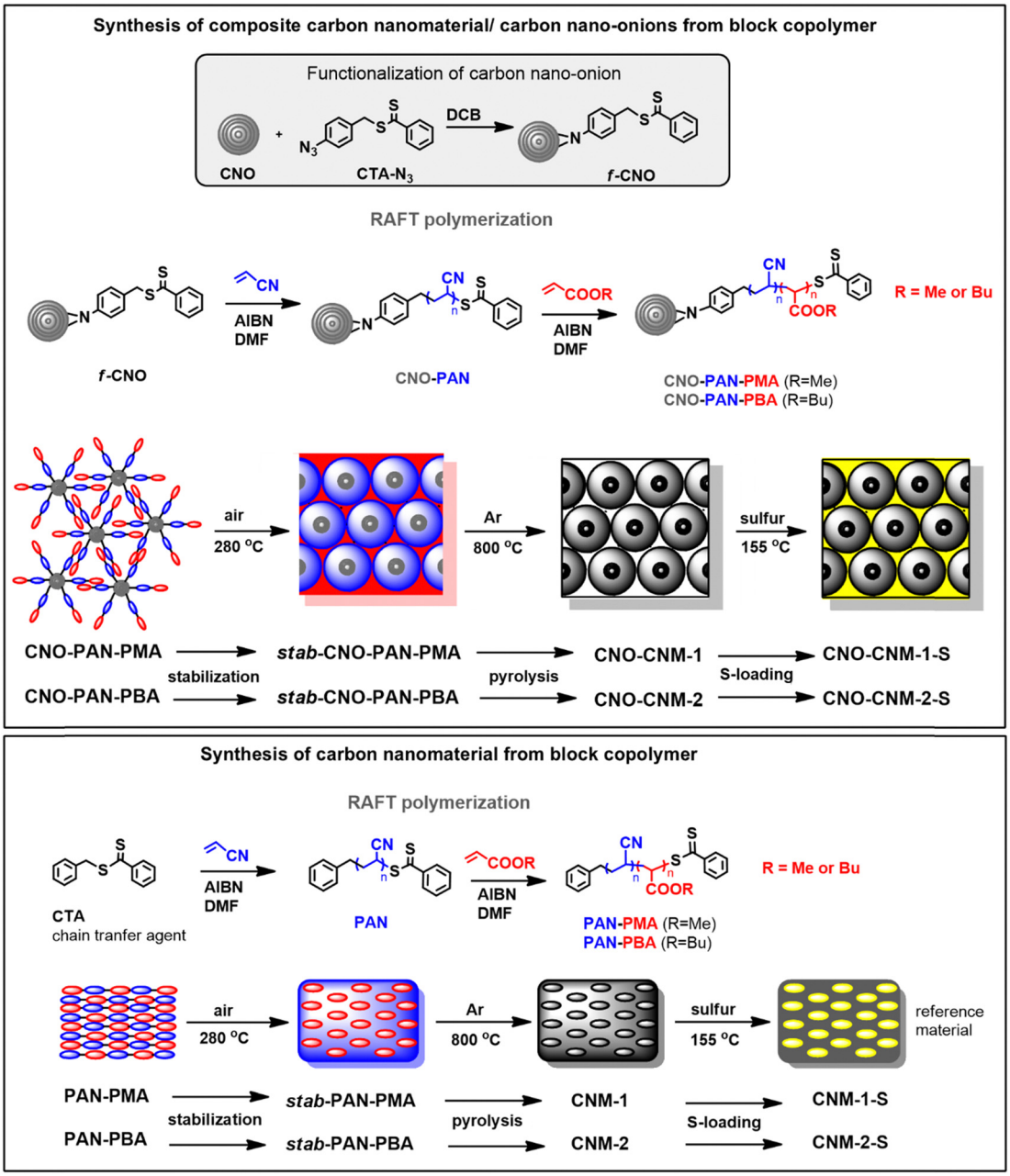

Fig. 1 Schematic representation of the synthesis of **CNM-1-S** and **CNM-1-S** and their hybrids with CNOs (**CNO**–**CNM-1-S** and **CNO**–**CNM-1-S**).

CNO should be used as low as possible to be a platform to hierarchically organize polymers on its surface and improve the properties of the obtained material. We previously checked that a very low content of CNOs in the carbon materials (*ca.* 5 wt%) allows for a significant improvement in their structural and electrochemical properties.[36] In another study of the carbon materials obtained from **PAN**-based 6-star polymers, a CNO content of as low as 2% was sufficient to enhance carbon properties.[35] Next, N-rich carbon nanomaterials were subjected to the reaction with sulfur to obtain N-doped carbon materials (**CNO–CNM-S**). Doping with sulfur was realized using a mixing–melting–diffusion process.[40,41] This straightforward method successfully confines pores with sulfur allotropes so there is no bulk sulfur in the mixture.[40]

Long heating time (20 hours) and slow heating rate (0.5 °C min^{-1}) were applied to ensure complete migration of sulfur into carbon nanomaterials.[42] A sufficient excess of sulfur was used to fill pores appropriately (the carbon/sulfur mass ratio was equal to 2 : 3).[41,42]

After that, the samples were heated for 30 minutes at 250 °C to remove sulfur from the surface of materials.[43,44] All sulfur–carbon samples have a sulfur loading of 51–57 wt%. The TG curves of materials before and after doping with sulfur are presented in Fig. 2. The sulfur contents in **CNM-1-S**, **CNM-2-S**,

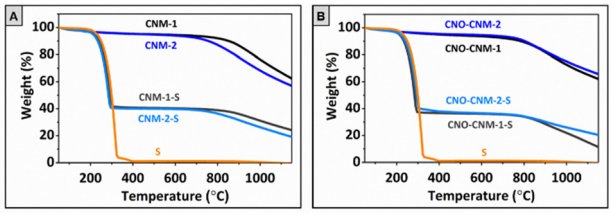

Fig. 2 TGA curves of the carbon nanomaterials (A) and their hybrids with CNOs (B) recorded in Ar.

CNO–CNM-1-S, and **CNO–CNM-2-S**, calculated based on the total weight losses at 500 °C, are 54, 55, 58, and 58 wt%, respectively. In general, these results are close to the calculated theoretical values of sulfur loading.

Spectroscopic studies of materials

Materials at each stage of the synthesis were analyzed using Fourier transform infrared (FTIR) spectroscopy (Fig. 3). The polymerization of AN (first block) was confirmed by the presence of a characteristic signal from the stretching vibrations of the CN group at 2240 cm^{-1} and the bands at about 2890, 1465, and 1250 cm^{-1} which are assigned to the aliphatic CH group vibrations of different modes in CH and CH_2.[45] In block polymers of **PAN**–poly(acrylic ester), characteristic signals of ester groups at C═O at about 1720 cm^{-1} and C–O at about 1140 cm^{-1} appeared (Fig. 3A).[46] Analogous signals are observed for CNO-based polymers (Fig. 3B). In addition, a comparison of the spectra of **CTA-N_3** and **f-CNO** revealed that **CTA-N_3** reacted with the C═C groups on the CNO's surface to form aziridine rings. Therefore the signal at 2130 cm^{-1} related to $-N_3$ group[47] disappeared in the **f-CNO** FTIR spectrum (Fig. 3B). After oxidative thermal treatment, characteristic signals from the nitrile group in the spectra of stabilized polymers (***stab*-PAN–PMA**, Fig. 3C, ***stab*-PAN–PBA**, Fig. 3D, ***stab*-CNO-PAN–PMA**, Fig. 3E, and ***stab*-CNO-PAN–PBA**, Fig. 3F) disappeared as a result of intramolecular cyclization of the linear structure, which leads to the formation of a ladder polymer and cross-linking of the CN groups.[48] New broad bands appeared in the region between 1630 and 1100 cm^{-1} that may indicate an oxidized N-doped graphitic structure formation.[49] The wide band at a range of 1630–1600 cm^{-1} can be attributed to the stretching vibration of C═C and highly conjugated form of the carbonyl group (quinone groups)[50] and at 1220 cm^{-1} to C–N stretching of aromatic amines in benzenoid units.[49] Moreover, an additional band at about 1050 cm^{-1} can be assigned to C–O stretching in ethers or epoxides.[51]

Further thermal treatment in inert gas and at 800 °C leads to the characteristic signals of the ester groups to disappear, resulting in the depolymerization of **PMA** or PBA and the

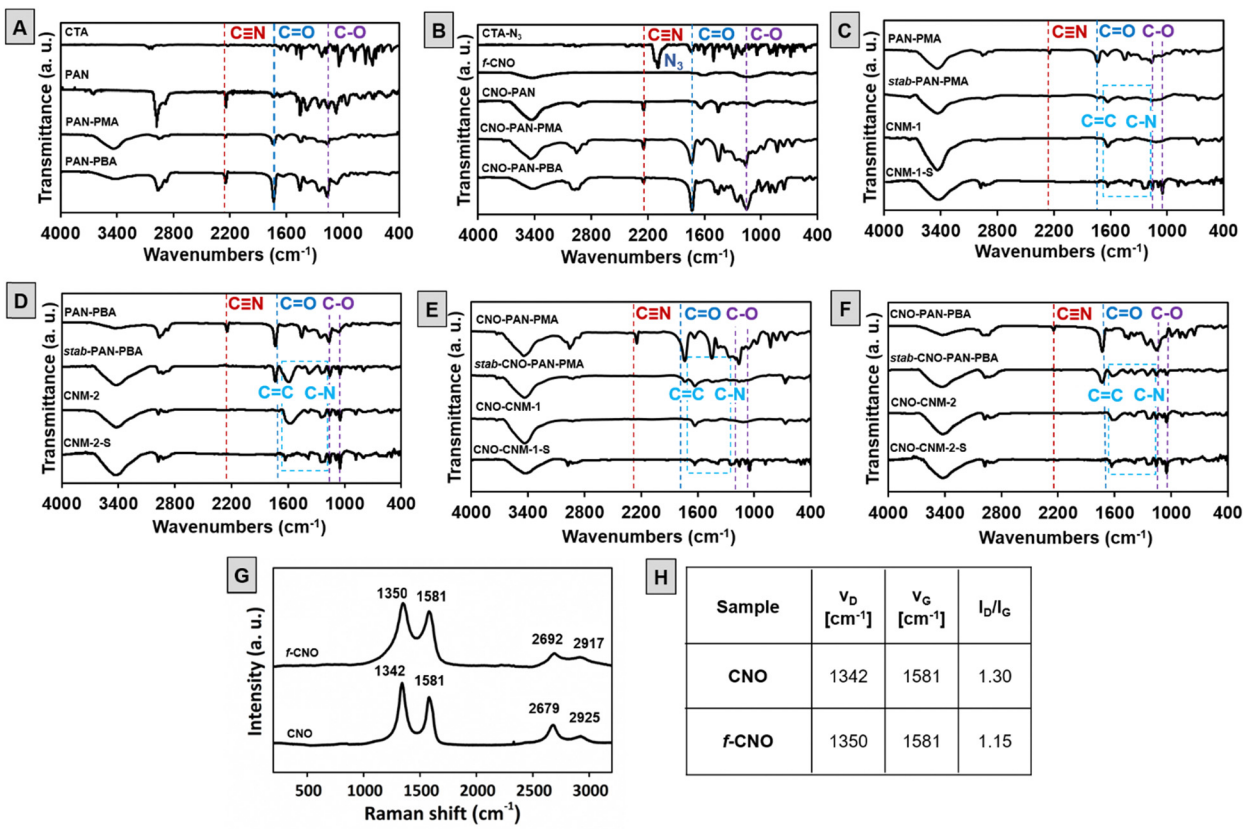

Sample	V_D [cm^{-1}]	V_G [cm^{-1}]	I_D/I_G
CNO	1342	1581	1.30
f-CNO	1350	1581	1.15

Fig. 3 (A)–(F) The FTIR spectra of a chain transfer agent, **PAN**–polymer, **PAN**–polyacrylate copolymers, and their composites before and after thermal treatment; (G) Raman spectra of CNO and **f-CNO**; and (H) the frequencies for the G and D bands and their relative intensities (I_D/I_G) for CNO and **f-CNO** excited at 514 nm.

formation of pyrolyzed materials without CNOs (**CNM-1** and **CNM-2**, Fig. 3C and D, respectively) or with CNOs (**CNO–CNM-1** and **CNO–CNM-2**, Fig. 3E and F, respectively). After sulfur loading, no additional bands exist in the spectra of all carbon nanomaterials (**CNM-1-S**, **CNM-2-S**, **CNO–CNM-1-S**, and **CNO–CNM-2-S**, Fig. 3C and F).

This indicates the incorporation of sulfur in the polymeric skeleton, but it does not change the structure of CNM. Before thermal treatment a broad band at about 3400 cm^{-1} is present, which can be attributed to the stretching vibrations of O–H and N–H groups and their intra- and intermolecular hydrogen bonding.[51,52]

The Raman spectra of **CNO** and **f-CNO** (Fig. 3G and H) show several characteristic bands at approximately 1350 (D band), 1580 (G band), 2680 and 2920 cm^{-1} (overtone and combination bands).[53,54] Most often, analysis of the intensity ratio of D and G bands (I_D/I_G), attributed to sp^3 and sp^2-hybridized carbon atoms, is used to characterize carbon graphitic materials and to confirm their further modifications.[37,55] A decrease in the I_D/I_G ratio, from 1.3 for pristine **CNO** to 1.15 for **f-CNO**, is observed (Fig. 3H). The reaction between CNOs and **CTA-N_3** leads to the formation of aziridine rings and, consequently, changes the hybridization of carbon atoms from sp^2 to sp^3. Simultaneously, the number of sp^2-hybridized carbon atoms increases due to the introduction of benzyl dithiobenzoate moieties.

In the mixing–melting–diffusion method, sulfur confines in pores with its allotropes and does not react with carbon structures to form carbon–sulfur bonds.[40] Therefore, carbon nanomaterials before loading with sulfur were characterized by X-ray photoelectron spectroscopy (XPS) to analyze their elemental composition. The XP spectra revealed the presence of carbon, oxygen, sulfur, and nitrogen. No sulfur peaks from the end groups of copolymers were observed in the spectrum, which confirmed their elimination in the pyrolysis process. However, it should be noted that after the mixing–melting–diffusion process with sulfur, additional loading of this element was recorded by the XPS method (Table S6, ESI†). Surface analysis was performed for **CNM-S-2**, and the percentage of sulfur was about 3%. The distribution of elements was defined due to the deconvolution of the high-resolution spectral C 1s, N 1s, S 2p, and O 1s regions. Table S6 (ESI†) shows the percentage contents of elements (C, N, O, and S). Nitrogen atoms occur intrinsically in **PAN**, and their concentration is approximately 6.73–7.34%, while oxygen atoms were formed during crosslinking under an air atmosphere, and their content is 4.2–5.22%.

Five peaks dominate in the deconvoluted C 1s spectra: those that correspond to C=C sp^2 at 284.4 eV, C–H sp^3 at 285 eV, C–C sp^3 at 285.6 eV, C–OH at 286.4 eV bonds of hybridized graphitic carbon[56] and peak at around 283.9 eV are attributed to the defects in carbon structure (Fig. S10 and Table S7, ESI†).[57] Other carbon peaks are in amounts less than 4% and can be attributed to carbon–oxygen single and double bonds in ether, ester, and acids (Table S7, ESI†).[35]

For the O 1s deconvoluted spectrum (Fig. S11 and Table S8, ESI†), the binding energies at 530.6 (± 0.2), 532.1 (± 0.2), 533.3 (± 0.2), and 535.0 6 (± 0.3) eV correspond to a highly conjugated form of carbonyl oxygen, such as quinone groups, phenolic C–OH,[58] ether groups C–O–C[59,60] and chemisorbed oxygen,[61] respectively, which indicates a material highly rich in oxygen atoms. These deconvoluted peaks may be associated with functional groups observed in FTIR analyses (Fig. 3), such as quinone-type conjugated C=O at 1630 cm^{-1}, ether C–O at 1050 cm^{-1}, or –OH at 3400 cm^{-1}.

The N 1s spectra were deconvoluted into four peaks verifying the existence of pyridinic nitrogen at 398 eV, pyrrolic nitrogen at 399.5 eV, graphitic nitrogen (quaternary nitrogen atoms coordinated in the graphene lattice in substitution of C) at 400.6 eV, and oxidized pyridinic oxide at 403 (± 0.1) eV (Fig. 4 and Fig. S11 and Table S9, ESI†).[44] The N 1s spectra of CNO-based nanomaterials contain a slightly larger amount of graphitic N, which provides an additional electron to delocalized π-systems. The content of pyridinic and pyrrolic N species for all materials is high and amounts to 35–40% and 15–19%, respectively.

It should be noted that the percentage content of chemical species in the deconvoluted C 1s, O 1s, and N 1s spectra for all synthesized carbon nanomaterials is quite similar. The main differences in the intensity of some peaks are visible for CNMs with and without CNOs. In the O 1s spectra after the addition of CNO, the peak corresponding to conjugated C=O increased

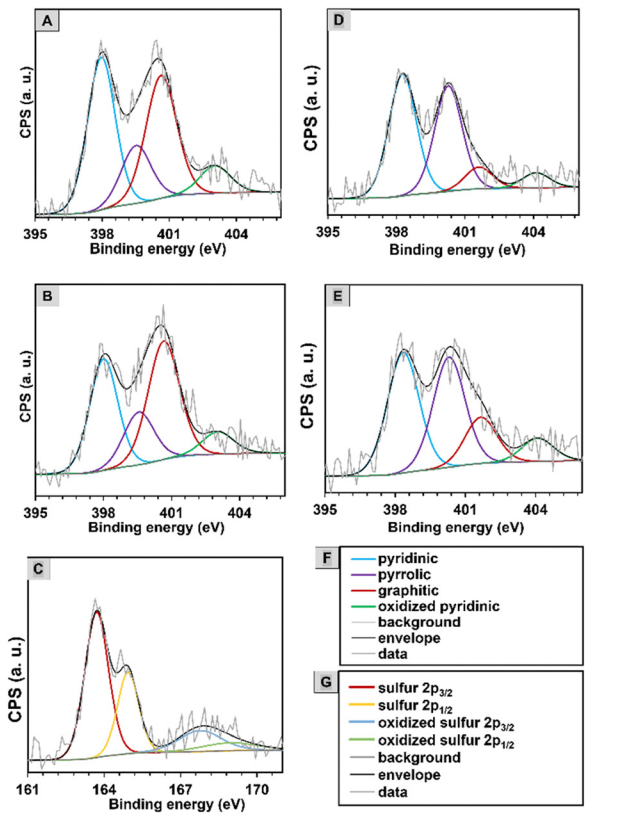

Fig. 4 XPS spectra of the N 1s spectral region of (A) **CNM-1** and (B) **CNO–CNM-1**, S 2p spectral regions of (C) **CNM-S-2**, N 1s spectral region of (D) **CNM-2** and (E) **CNM-S-2**, (F) legend of nitrogen spectra, and (G) legend of the sulfur spectrum.

(from 5.7 to 20.6% for the **PMA**-derived material and from 7.6 to 24.2% for the **PBA**-derived one). In comparison, the peak assigned to C–O decreased (by an average of 15%).

In the S 2p spectrum (Fig. 4C), S 2p is deconvoluted into two peaks at binding energies of 163.7 and 164.9 eV that are assigned to S $2p_{3/2}$ and S $2p_{1/2}$.[62] The characteristic S 2p peaks are assigned to S_8 molecules, that are formed in the mixing–melting–diffusion process in mesoporous carbon materials.[62] At higher energies of 167.8 and 168.9 eV, the deconvoluted peaks confirmed the presence of sulfates, the oxidized form of S $2p_{3/2}$ and S $2p_{1/2}$ (Table S10, ESI†).[63]

Morphological and textural characterization of materials

The materials' morphology was examined by scanning electron microscopy (SEM). The images for polymers before and after thermal treatment with and without CNOs are shown in Fig. 5. Stabilization in air converted materials into cyclized network structures with reduced polymer chain mobility (***stab*-PAN–PMA** and ***stab*-CNO-PAN–PMA**).[64] Pyrolysis removed all the **PMA** domains and produced pores in the carbon materials; therefore, all carbon materials had rough surfaces.[65] **CNM** synthesized with and without CNOs showed variations in the morphology and particle size. CNOs constitute a platform for polymeric chain growth. Although in some SEM images, the material forms spherical nanoparticles, it should be noted that it is not a homogeneous material forming spherical particles, such as the core–shell type. It should be emphasized that carbon nanostructures in the reaction solvent form nanostructured aggregates even after functionalization. Therefore, CNO aggregates of different sizes are modified with polymer chains. We applied reversible addition–fragmentation chain-transfer polymerizations to control the polymerization process and to obtain polymers with predefined molecular weights. All steps were performed carefully and precisely, but despite our efforts, the obtained material revealed morphological variability. It is evident in Fig. 5 when the polymer material is compared with the composite (**CNM-1** and **CNO–CNM-1**). However, it should be emphasized that the addition of CNOs positively affects the change in the material's morphology, leading to increased porosity. In the case of **CNO–CNM-1**, a spherical structure appeared; however, the size of the particles was not sufficiently uniform, ranging from 1–10 μm. In the ESI,† we have compiled SEM images for all materials obtained after pyrolysis (Fig. S13, ESI†). Although the morphology of the materials after pyrolysis is very similar, the most developed surfaces are shown by materials with sulfur addition, **CNO–CNM-S-1** and **CNO–CNM-S-2**. EDAX-SEM analysis for the pyrolyzed materials indicates a uniform distribution of elements in the obtained materials (Fig. S14, ESI†).

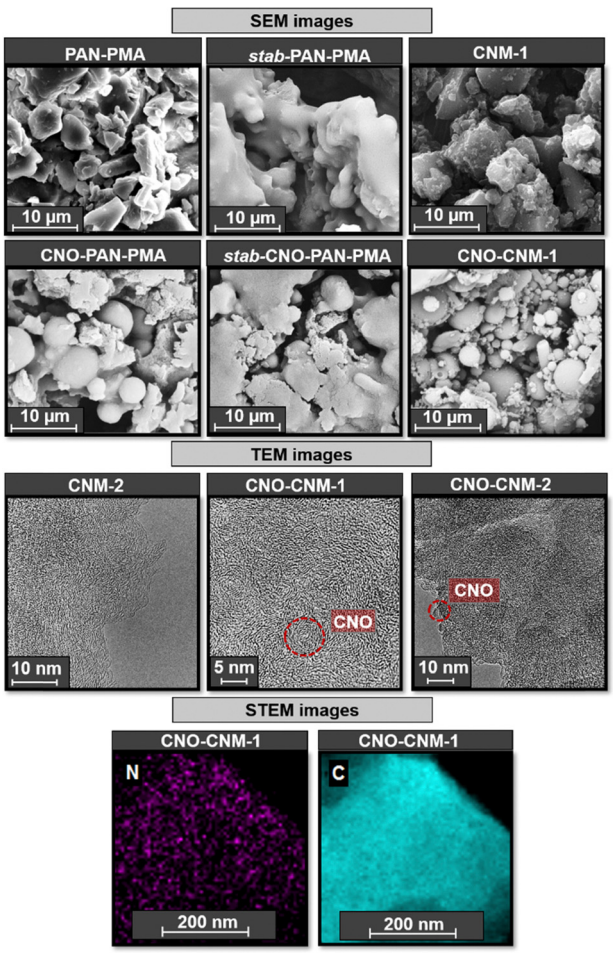

Fig. 5 SEM of **CNM-1** and **CNO–CNM-1** before and after thermal treatment, HRTEM of carbon nanomaterials, and STEM-EDX elemental map of **CNO–CNM-1**.

SEM observations are conducted at the micro level, while the pores are only visible at the nanoscale. Therefore, high-resolution transmission electron microscopic (HRTEM) studies were performed to analyze the carbon materials (Fig. 5) and it was found that the structure was slightly graphitic.[17]

HRTEM confirmed the removal of poly(acrylic esters) and converting **PAN–PMA** or **CNO-PAN–PMA** into more porous carbon materials. All materials have uniformly distributed spherical cavities in the structure (Fig. 5). The carbon structure became increasingly ordered after the addition of CNOs.

Scanning transmission electron microscopy (STEM) combined with energy dispersive X-ray spectroscopy (EDX) was used to assess the type and arrangement of atoms constituting the synthesized materials (Fig. 5). STEM-EDX maps recorded after scanning the surface of **CNO–CNM-1** show a uniform distribution of C and N atoms in the material, with a quantitative predominance of the former.

However, Fig. 5 denotes areas with high amounts of N (marked in purple) and the shaded regions that indicate a lack of N. The specific surface area (S_{BET}) and textural parameters of **CNM-1**, **CNM-2**, **CNO–CNM-1**, and **CNO–CNM-2** were calculated based on N_2 adsorption measurements (Fig. 6 and Table 1). All recorded curves with noticeable hysteresis loop (Fig. 6A) represent type IV isotherms, indicating the dominance of mesopores (2–50 nm) in the series of synthesized materials.[66,67] However, the difference in the hysteresis loop shape is observed in **CNM-1** and **CNM-2** structures, suggesting the different shapes of the pores in the materials. The isotherm corresponding to

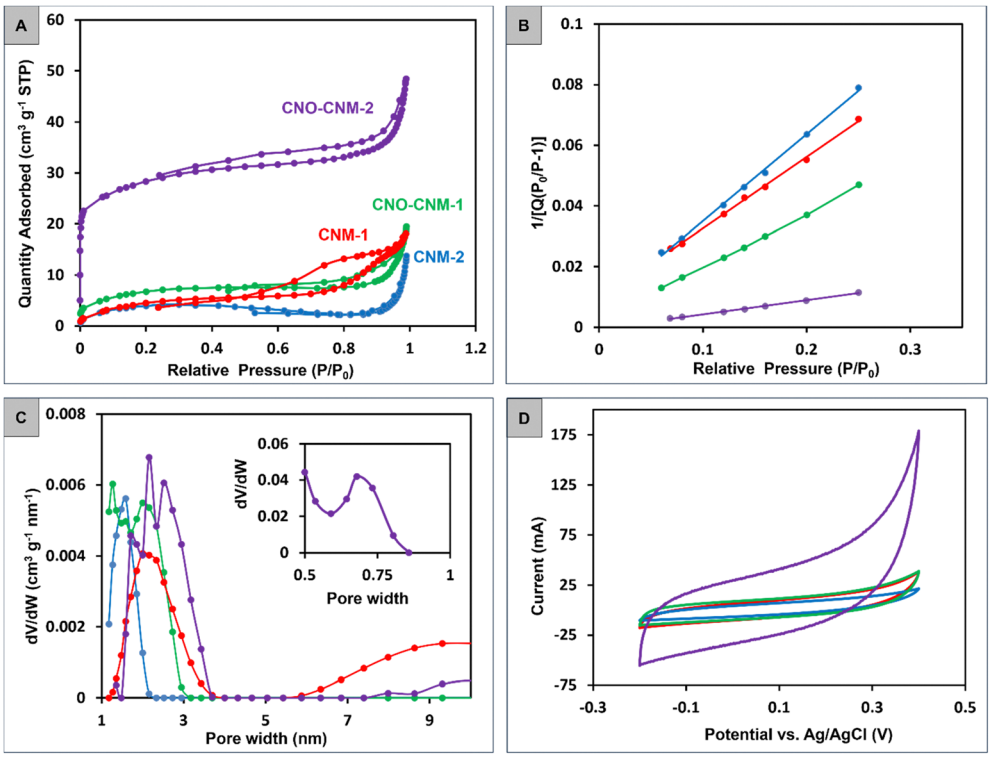

Fig. 6 (A) N_2 adsorption–desorption isotherms of the synthesized materials with corresponding (B) BET curves and (C) differential pore size distributions based on DFT calculations. (D) CV curves of GCE electrodes modified with the synthesized materials recorded in 1 M KOH at a scan rate of 50 mV s^{-1}.

CNM-1 is characterized by the H2-type hysteresis loop, indicating the occurrence of cylindrical pores with an ink-bottle shape.[66] The H3-type hysteresis loop observed in the course of the **CNM-2** isotherm, in turn, proves the existence of wedge-shaped mesopores.[66] The reason for these differences is the different lengths of poly(acrylic ester) chains involved in the backbone formation of each structure before their pyrolysis. Interestingly, a similar relationship was not observed between analogous CNO-containing materials. Isotherms recorded for **CNO–CNM-1** and **CNO–CNM-2** in both cases indicate the dominance of wedge-shaped pores.

The values of the specific surface area (S_{BET}) of **CNM-1**, **CNM-2**, and **CNO–CNM-1** (Table 1), determined from Brunauer–Emmett–Teller (BET) curves (Fig. 6B), are similar, and their values are within the range of 18–25 m^2 g^{-1}. A significant increase of S_{BET} is observed for **CNO–CNM-2** (94 m^2 g^{-1}), indicating that this material has different textural behavior. A *t*-plot analysis to assess the proportion of meso- to micropores confirmed that only for the **CNO–CNM-2** system is the area occupied by micropores remarkable (S_{micro} = 48 m^2 g^{-1}) (Table 1). It suggests immobilizing longer **PBA** chains on the **CNO-PAN** surface that creates a micro-mesoporous structure. The micro-mesoporous behavior of **CNO–CNM-2** is also confirmed by Barrett–Joyner–Halenda (BJH) (Table 1) and density functional theory (DFT) calculations (Fig. 6C). The average pore diameters of **CNO–CNM-1** and **CNO–CNM-2** decrease relative to the values for **CNM-1** and **CNM-2**, respectively (Table 1). In contrast, their cumulative pore volume increases. The pore size distribution analysis also indicates the presence of both mesopores (Fig. 6C) and micropores (inset Fig. 6C) in the **CNO–CNM-2** structure.

It should be emphasized that although longer PBA chains are present in the composite material during its formation, this polymer component is removed during pyrolysis. **PAN** intramolecularly cyclized during thermal treatment (stabilization and pyrolysis processes) of the diblock **PAN**–poly(acrylic ester)

Table 1 Textural parameters of the synthesized materials calculated from N_2 adsorption measurements

Material	S_{BET} (m^2 g^{-1})	S_{micro} [a] (m^2 g^{-1})	S_{ext} [ab] (m^2 g^{-1})	Cumulative volume of pores[c] (cm^3 g^{-1})	Average pore diameter[c] (nm)	C_s (F g^{-1})
CMN-1	23	0	23	0.0194	22	8
CMN-2	18	0	18	0.0164	57	5
CNO–CMN-1	25	2	23	0.0234	12	9
CNO–CMN-2	94	48	46	0.0420	6	32

[a] Calculated using the *t*-plot method. [b] ext = external. [c] Calculated using the BJH method.

copolymer, transforming its linear structure into a cross-linked ladder structure. At the same time, acrylic esters are removed, forming pores in the materials. Therefore, carbon surfaces do not consist of acrylic (*e.g.*, PBA) chains. However, the polymer's structure before heating was carefully studied, and the presence of acrylic parts was confirmed unambiguously by NMR and IR spectra (Fig. 3). Moreover, the covalent functionalization of CNO with a chain transfer agent was confirmed by Raman spectra, which proved that polymers are organized on the surface of CNO *via* a covalent C–N bond. The significant increase in S_{BET} for **CNO–CNM-2** is attributed to the better organization of polymer (that forms pores in the pyrolysis process) on the surface of CNO.

Electrochemical performance of polymer-derived N-doped carbon nanomaterials

Cyclic voltammetry (CV) curves recorded for all materials (Fig. 6D) showed a relatively low capacitive nature. The specific capacitance (C_s) values (Table 1) were calculated from the formula:

$$C_s = \frac{\int_{V_1}^{V_2} i(V)\mathrm{d}V}{2vm(V_2 - V_1)}$$

where i – current, v – scan rate, m – mass of material, and V – potential. The obtained C_s values correlate well with the S_{BET} values. The **CNO–CNM-2** structure, which shows the highest S_{BET}, also exhibits the highest C_s value (32 F g^{-1}). Comparing the series **CNM-1** and **CNO–CNM-1**, and **CNM-2** and **CNO–CNM-2**, the difference in the capacitance values between pure polymers and composites (after adding CNO) is significant in the case of the second series. A substantial change in the textural properties of the material was noted (Table 1). For **CNO–CNM-2**, a significant decrease in the average pore diameter was observed from 57 to 6 nm, with a simultaneous increase in S_{micro} from O to 48 m^2 g^{-1} and a 2.5-fold increase in the cumulative volume of pores. Consequently, the C_s value for **CNM-2** and **CNO–CNM-2** increased from 5 to 32 F g^{-1}, respectively. For the **CNM-1** and **CNO–CNM-1** series, no significant changes in textural properties were observed, and at the same time, the C_s value remained unchanged.

The four synthesized carbon–sulfur composites were used as positive electrodes in the Li–S batteries. The tested systems were labeled after the composites as **CNM-1-S**, **CNM-2-S**, **CNO–CNM-1-S**, and **CNO–CNM-2-S**. The discharge curves of all batteries (Fig. 7A) feature a voltage plateau at around 2.1 V. This value is generally attributed to the sulfur reduction to short-chain polysulfides (*e.g.*, Li_2S) through a rapid reduction of intermediate, higher-order polysulfides (Li_2S_x where $x \geq 4$).[26] Since no other plateaus are distinguishable at higher voltages, it suggests that the encapsulation of sulfur in carbon hinders the diffusion of the soluble higher-order polysulfides to the electrolyte, which was noted by other reports as well.[68] The cells with CNOs as a part of the electrode material exhibit longer and

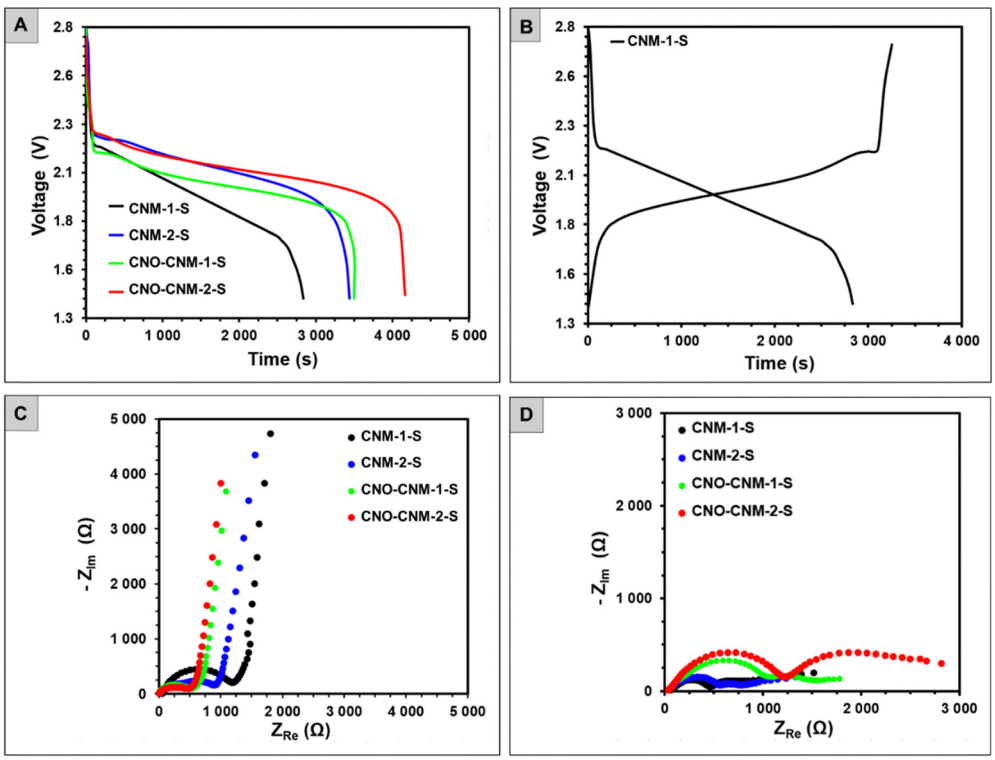

Fig. 7 Discharge curves of the Li–S batteries with four different cathode materials (A) with an example of charge/discharge profiles for **CNM-1-S** cathode (B) recorded at the rate of C/20. Nyquist plots of the Li–S batteries with four different cathode materials after the cell assembly (C) and after the first charging process (D) the electrolyte was 1 M LiTFSA in DOL/DME (1 : 1 v/v).

less steep voltage plateau, and they can deliver the discharge capacity of 81.4 and 96.8 mA h g^{-1} for **CNO–CNM-1-S** and **CNO–CNM-2-S**, respectively.

The **CNO–CNM-2-S**, with its 18.9% higher discharge capacity due to a higher sulfur doping, is a significant finding in our research. Similarly, the discharge capacity of sulfur-rich **CNM-2-S** equaled 80.1 mA h g^{-1}, and it was 21.5% higher than that of **CNM-1-S** (65.9 mA h g^{-1}). CNOs in the cathode material affected not only the shape of the Li–S batteries' discharge profiles but also increased the discharge capacity to a similar extent as the sulfur content.

Comparing the battery pair with the same sulfur content (**CNM-1-S** *vs.* **CNO–CNM-1-S** and **CNM-2-S** *vs.* **CNO–CNM-2-S**), the ones with **CNO–CNM** nanomaterial supplied over 20% higher capacity than their **CNM** counterparts. The S_{BET} values revealed that **CNO–CNM**-based materials possessed a more developed S_{BET}. A greater surface area likely facilitated access to more electrochemically active sulfur for faradaic reactions.

The difference between the amount of charge supplied during charging and delivered upon discharging (Fig. 7B) was relatively low for all batteries, indicating a low irreversible capacity and high current efficiency. After assembly at the open circuit voltage (Fig. 7C), Nyquist plots of the Li–S batteries consisted of a semi-circle in the high-frequency region, followed by an inclined line at medium and low frequencies.

The semi-circle resistances slightly exceed 500 Ω for **CNO–CNM-1-S** and **CNO–CNM-2-S**, whereas they reach as high as 1200 and 960 Ω for **CNM-1-S** and **CNM-2-S**. In a charged state (Fig. 7D), two semi-circles appeared from high to low frequencies, followed by a bent line. Besides the real part of impedance Z_{RE} (resistance) grew, while the imaginary part Z_{IM} became much lower compared to the impedance spectra of the freshly assembled cells. The total resistance of the charged Li–S batteries ranged from 1330 Ω (**CNM-2-S**) to 2800 Ω (**CNO–CNM-2-S**). Such values are pretty high, although not uncommon for a charged state.[69] Typically, though, the total resistance in the 100–250 Ω range would accompany the reversible cycling of Li–S batteries.[70] The slightly overlapping semi-circles indicate that several parallel processes might occur (*e.g.*, related to SEI formation on the anode and partial oxidation of polysulfides at the cathode).

Experimental

Materials

The CNOs were obtained by the modified Kuznetsov method by annealing treatment of ultradispersed nanodiamond powder with a crystal size between 4 and 6 nm (Carbodeon μDiamond®Molto, 97 wt%).[71,72] *N*,*N*-Dimethylformamide (DMF, POCH S.A., Poland) was distilled over phosphorus pentoxide (P_2O_5, pure, Honeywell, USA). 2,2′-Azobis(2-methylpropionitrile) (AIBN, ≥95%, POL-AURA, Poland) was recrystallized from methanol (MeOH, Chempur, Poland) before use. Acrylonitrile (≥99%, Aldrich, Germany), methyl acrylate (≥99%, Aldrich, Germany), and butyl acrylate (≥99%, Aldrich, Germany) were filtered through neutral alumina (Merck, Germany) before use. Sulfur sublimed (99.9%, Chempur, Poland) was used as received. The CNOs, potassium bromide (≥ 99%, Aldrich, Germany), and glassware were dried in a furnace at 120 °C overnight before use. The deuterated solvent dimethylsulfoxide (DMSO-d_6) was purchased from Euroisotop (United Kingdom). In electrochemical measurements, an organic solution of lithium bis(trifluoromethane sulfonyl)amide (LiTFSA, 97%, Merck, Germany) in 1,3-dioxolane (DOL, anhydrous, 99.8%, Merck, Poland) and 1,2-dimethoxyethane (DME, anhydrous, 99.5%, Merck, Germany) was prepared and used without further purification. Battery-grade conductive carbon black (C65, Imerys), poly(vinylidene fluoride) (PVDF, Solvay), and *N*-methylpyrrolidone (NMP, Fluka) were used for the preparation of the cathodes (working electrodes). The cathode material was coated on the Al current collector (thickness 0.2 mm, Nanoshel, United Kingdom), while the counter electrode was made of Li foil (thickness 0.2 mm, Nanoshel, United Kingdom). GF/A glass microfiber (Whatman) was used as a separator.

Synthesis procedures

Functionalized carbon nano-onions (f-CNOs). CNOs (30 mg) were suspended in anhydrous DCB (5 mL) under Ar and sonicated for 30 min. CTA-N_3 (120 mg, 0.42 mmol) was added and the reaction mixture was stirred for 12 h at reflux. Then the **f-CNOs** were filtered off, and washed with toluene, and hexane, followed by drying *in vacuo* affording 37 mg of the product as black powder.

Polyacrylonitrile (PAN). Benzyl dithiobenzoate (78 mg, 0.32 mmol), AN (4.19 mL, 64 mmol, 200 units), and AIBN (33 mol%, 17 mg) were dissolved in DMF (12 mL) and Ar was bubbled through this suspension for 15 min. The reaction mixture was stirred for 24 h at 70 °C under Ar. The polymers were then precipitated with MeOH, followed by filtration and drying on a vacuum pump, affording the product as a white powder (2.98 g) in 86% yield. ^{1}H NMR (500 MHz, DMSO-d_6, ppm) characteristic signals: δ = 3.13 (m, 1H, –CH_2CHCN), 2.04 (m, 2H, –CH_2CHCN); IR (ATR, cm^{-1}): $\tilde{\nu}$ = 3640 (m), 2941 (s), 2243 (m) (–CN), 1606 (w).

CNO-based polyacrylonitrile (CNO-PAN). First, **f-CNOs** (10 mg) were suspended in a solution of AIBN (0.03 mmol, 5 mg) and AN (19 mmol, 1.24 mL) in anhydrous DMF (4 mL) under Ar was sonicated for 30 min. Ar was bubbled through this suspension for 15 min. The reaction mixture was stirred for 24 h at 70 °C under Ar. The polymers were then precipitated with MeOH, followed by filtration and drying on a vacuum pump, affording the product as a grey powder 978 mg in 97% yield. ^{1}H NMR (500 MHz, DMSO-d_6, ppm) characteristic signals: δ = 3.18 (m, –CH_2CHCN), 2.04 (m, –CH_2CHCN); IR (ATR, cm^{-1}): $\tilde{\nu}$ = 3410 (s), 2935 (s), 2247 (m) (–CN), 1627 (w).

Block copolymer PAN–PMMA. PAN polymer (1000 mg, 0.092 mmol), MA (1.7 mL, 18 mmol, 200 units), and AIBN (33 mol%, 5 mg) were dissolved in DMF (8 mL) and Ar was bubbled through this suspension for 15 min. The reaction mixture was stirred for 24 h at 70 °C under Ar. The polymers were then precipitated with MeOH, followed by filtration and

drying on a vacuum pump, affording the product as a white powder (1.51 g) in a 58% yield. ^{1}H NMR (500 MHz, DMSO-d_6, ppm) characteristic signals: δ = 3.58 (s, OCH_3), 3.14 (m, –CH$_2$CHCN), 2.04 (m, –CH_2CHCN, CH$_2$CHCOOMe), 1.61 (m, –CH_2CHCOOMe); IR (ATR, cm^{-1}): $\tilde{\nu}$ = 3446 (s), 2965 (m), 2239 (w) (–CN), 1741 (s) (C═O), 1165 (s) (C–O).

Block copolymer PAN–PBA. PAN polymer (1000 mg, 0.092 mmol), BA (2.7 mL, 18 mmol, 200 units), and AIBN (33 mol%, 5 mg) were dissolved in DMF (10 mL) and Ar was bubbled through this suspension for 15 min. The reaction mixture was stirred for 24 h at 70 °C under Ar. The polymers were then precipitated with MeOH, followed by filtration and drying on a vacuum pump, affording the product as a white powder (1.75 g) in a 52% yield. ^{1}H NMR (500 MHz, DMSO-d_6, ppm) characteristic signals: δ = 3.92 (OCH_2), 3.13 (m, –CH$_2$CHCN), 2.05 (m, –CH_2CHCN, CH$_2$CHCOOBu), 1.53 and 1.32 (2m, –CH_2CHCOOBu, –CH_2CH_2–), 0.87 (m, –CH_3); IR (ATR, cm^{-1}): $\tilde{\nu}$ = 3430 (m), 2958 (s), 2260 (m) (–CN), 1737 (vs) (C═O), 1164 (s) (C–O).

CNO-based copolymer PAN–PMA (CNO-PAN–PMA). CNO-PAN (500 mg) was suspended in a solution of AIBN (0.015 mmol, 2.5 mg) and MA (9 mmol, 0.81 mL) in DMF (2 mL). Ar was bubbled through this suspension for 15 min., followed by sonication for 30 min. Next, the reaction mixture was stirred for 24 h at 70 °C. After cooling, the polymer was precipitated to MeOH affording 860 mg of the product as a grey powder in a 66% yield. ^{1}H NMR (500 MHz, DMSO-d_6, ppm) characteristic signals: δ = 3.58 (s, OCH_3), 3.17 (m, –CH$_2$CHCN), 2.04 (m, –CH_2CHCN, CH$_2$CHCOOMe), 1.61 (m, –CH_2CHCOOMe); IR (ATR, cm^{-1}): $\tilde{\nu}$ = 3442 (s), 2965 (m), 2239 (w) (–CN), 1741 (s) (C═O), 1167 (s) (C–O).

CNO-based copolymer PAN–PBA (CNO-PAN–PBA). CNO-PAN (500 mg) was suspended in a solution of AIBN (0.015 mmol, 5 mg) and BA (9 mmol, 1.29 mL) in DMF (4 mL). Ar was bubbled through this suspension for 15 min., followed by sonication for 30 min. Next, the reaction mixture was stirred for 24 h at 70 °C. After cooling, the polymer was precipitated to MeOH affording 890 mg of the product as a grey powder in a 68% yield. ^{1}H NMR (500 MHz,DMSO-d_6, ppm) characteristic signals: δ = 3.95 (OCH_2), 3.13 (m, –CH$_2$CHCN), 2.05 (m, –CH_2CHCN, CH$_2$CHCOOBu), 1.52 and 1.33 (2m, –CH_2CHCOOBu, –CH_2CH_2–), 0.88 (m, –CH_3); IR (ATR, cm^{-1}): $\tilde{\nu}$ = 3438 (m), 2965 (m), 2238 (w) (–CN), 1750 (vs) (C═O), 1164 (s) (C–O).

Stabilization and pyrolysis. All the **PAN**-derived polymers and hybrids were heated to 280 °C with a ramping rate of 1 °C min^{-1}, followed by stabilization for 1 h at 280 °C with a constant airflow. Then, the samples were cooled down to RT with a ramping rate of 10 °C min^{-1} with a constant Ar flow. Next, stabilized materials were heated to 800 °C with ramping rate of 10 °C min^{-1}, and pyrolyzed for 30 minutes at 800 °C in a constant Ar flow. Next, the samples were cooled down to RT with a ramping rate of 10 °C min^{-1} with constant Ar flow.

Carbon nanomaterials were obtained in the following yields: **CNM-1** from **PAN–PMA** copolymer 217 mg (57% weight loss); **CNM-2** from **PAN–PBA** copolymer 204 mg (59% weight loss); **CNO–CNM-1** from **CNO-PAN–PMA** copolymer 180 mg (64% weight loss); **CNO–CNM-2** from **CNO-PAN–PBA** copolymer 169 mg (66% weight loss).

Sulfur loading. The carbon nanomaterial (50 mg) was ground in an agate mortar with elemental sulfur (75 mg) for 15 minutes. The mixture was transferred to a test tube under an Ar atmosphere and the tube was vacuum sealed. Then it was heated in a tube furnace for 20 h at 155 °C (heating rate 0.5 °C min^{-1}). After cooling, the material was removed from the test tube and ground thoroughly in the mortar, then heated under an Ar atmosphere at 250 °C for 30 minutes, obtaining S-loaded carbon nanomaterials in the following yields (calculated S loading given in parenthesis): **CNM-1-S** 102 mg (51 wt% S); **CNM-2-S** 112 mg (55 wt% S); **CNO–CNM-1-S** 113 mg (56 wt% S); and **CNO–CNM-2-S** 116 mg (57 wt% S).

Conclusion

This work reported the successful synthesis of porous N-rich CNMs organized on a CNO surface. RAFT polymerization enabled the efficient synthesis of block copolymers consisting of PAN and poly(acrylic esters) with a specific carbon chain length. The PAN domains were stabilized in air flow, and the acrylic sacrificial block was removed by pyrolysis, leaving pores of defined sizes. The pore size was found to depend on the acrylic ester used. Sulfur was introduced into the pores, resulting in materials that contained approximately 51–57% of this element by weight. All materials exhibited evenly distributed spherical cavities in their structure, and after the addition of CNOs, the carbon structure became increasingly ordered. Additionally, these materials are characterized by a more developed surface area with micro-mesoporous characteristics, which influence the electrochemical properties of the material in faradaic reactions. The presence of electron-donating lone pairs in the pyridinic and pyrrolic N atoms can ensure a bond between N atoms and Li cations, effectively reducing the shifting effect by preventing the diffusion of polysulfides into the electrolyte.

The addition of even a tiny amount of CNOs to CNMs influenced the shape of the discharge profiles of Li–S batteries and also increased the discharge capacity. The CNO-based nanomaterial battery provided over 20% greater capacity than **CNM-1-S** and **CNM-2-S.** Based on our results, using CNO as a platform in the simple and repeatable synthesis of PAN-based carbons opens up new design possibilities for the cathode material in Li–S batteries.

Author contributions

Conceptualization, methodology, supervision, project administration, visualization, data curation and funding acquisition: M. E. P.-B. Methodology, visualization, validation, formal analysis and investigation: A. H., G. S., J. B., K. H. M., A. G. and G. L. The manuscript was written through contributions from all authors. All authors have given approval to the final version of the manuscript.

Data availability

The data supporting this article have been included as part of the ESI.† Raw experimental data are available from the corresponding author upon reasonable request.

Conflicts of interest

There are no conflicts to declare.

Acknowledgements

The authors gratefully acknowledge the financial support from the National Science Centre, Poland, grant UMO-2017/25/B/ST5/01414 and the Medical University of Bialystok, grant B.SUB.24.314 to M.E.P.-B. The authors also gratefully acknowledge Prof. Luis Echegoyen from the University of Texas at El Paso for providing the CNOs. The research was carried out with the equipment purchased thanks to the financial support from the European Regional Development Fund (POIG.02.01.00-06024/09, Maria Curie-Sklodowska University, Poland).

References

1 A. K. Thakur, K. Kurtyka, M. Majumder, X. Yang, H. Q. Ta, A. Bachmatiuk, L. Liu, B. Trzebicka and M. H. Rummeli, *Adv. Mater. Interfaces*, 2022, **9**, 2101964.
2 H. Wang, Y. Shao, S. Mei, Y. Lu, M. Zhang, J. Sun, K. Matyjaszewski, M. Antonietti and J. Yuan, *Chem. Rev.*, 2020, **120**, 9363–9419.
3 J. Zhu, T. Feng, X. Du, J. Wang, J. Hu and L. Wei, *J. Power Sources*, 2017, **346**, 120–127.
4 L. Sui, Y. Wang, W. Ji, H. Kang, L. Dong and L. Yu, *Int. J. Hydrogen Energy*, 2017, **42**, 29820–29829.
5 Z.-A. Liu, Y. Tao, X.-Z. Song, M. Bao and Z. Tan, *RSC Adv.*, 2017, **7**, 6664–6670.
6 X. Chen, S. Wang, Y. Wang, Z. Yang, S. Liu, J. Gao, Z. Su, P. Zhu, X. Zhao and G. Wang, *Electrocatalysis*, 2019, **10**, 277–286.
7 N. Wang, H. Tian, S.-Y. Zhu, D.-Y. Yan and Y.-Y. Mai, *Chinese J. Polym. Sci.*, 2018, **36**, 266–272.
8 M. Mi, X. Liu, W. Kong, Y. Ge, W. Dang and J. Hu, *Desalination*, 2019, **464**, 18–24.
9 F. Liu, J. Niu, X. Chuan and Y. Zhao, *J. Alloys Compd.*, 2023, **947**, 169654.
10 L. Xing, C. Song and A. Kong, *J. Solid State Chem.*, 2020, **287**, 121348.
11 K. Qu, Y. Zheng, S. Dai and S. Z. Qiao, *Nano Energy*, 2016, **19**, 373–381.
12 Z. Xu, L. Li, X. Chen and G. Xiao, *ACS Appl. Energy Mater.*, 2021, **4**, 1954–1961.
13 W. Kiciński, M. Szala and M. Bystrzejewski, *Carbon*, 2014, **68**, 1–32.
14 Y. Gao, Q. Wang, G. Ji, A. Li and J. Niu, *RSC Adv.*, 2021, **11**, 5361–5383.
15 E. Cipriani, M. Zanetti, P. Bracco, V. Brunella, M. P. Luda and L. Costa, *Polym. Degrad. Stab.*, 2016, **123**, 178–188.
16 C. K. Kim, H. Zhou, T. Kowalewski, K. Matyjaszewski and H. K. Kim, *ACS Appl. Mater. Interfaces*, 2019, **11**, 2093–2102.
17 R. Yuan, M. Kopeć, G. Xie, E. Gottlieb, J. W. Mohin, Z. Wang, M. Lamson, T. Kowalewski and K. Matyjaszewski, *Polymer*, 2017, **126**, 352–359.
18 J. P. McGann, M. Zhong, E. K. Kim, S. Natesakhawat, M. Jaroniec, J. F. Whitacre, K. Matyjaszewski and T. Kowalewski, *Macromol. Chem. Phys.*, 2012, **213**, 1078–1090.
19 T. Liu and G. Liu, *J. Mater. Chem. A*, 2019, **7**, 23476–23488.
20 J. M. Serrano, T. Liu, A. U. Khan, B. Botset, B. J. Stovall, Z. Xu, D. Guo, K. Cao, X. Hao, S. Cheng and G. Liu, *Chem. Mater.*, 2019, **31**, 8898–8907.
21 N. P. Truong, G. R. Jones, K. G. E. Bradford, D. Konkolewicz and A. Anastasaki, *Nat. Rev. Chem.*, 2021, **5**, 859–869.
22 J. Tanaka, N. E. Archer, M. J. Grant and W. You, *J. Am. Chem. Soc.*, 2021, **143**, 15918–15923.
23 H. Yang, J. Chen, J. Yang and J. Wang, *Angew. Chem., Int. Ed.*, 2020, **59**, 7306–7318.
24 S. Evers and L. F. Nazar, *Chem. Commun.*, 2012, **48**, 1233–1235.
25 K. Mi, Y. Jiang, J. Feng, Y. Qian and S. Xiong, *Adv. Funct. Mater.*, 2016, **26**, 1571–1579.
26 S. Choudhury, M. Zeiger, P. Massuti-Ballester, S. Fleischmann, P. Formanek, L. Borchardt and V. Presser, *Sustainable Energy Fuels*, 2017, **1**, 84–94.
27 W. Jan, A. D. Khan, F. J. Iftikhar and G. Ali, *J. Energy Storage*, 2023, **72**, 108559.
28 M. E. Plonska-Brzezinska and L. Echegoyen, *J. Mater. Chem. A*, 2013, **1**, 13703.
29 S. Sek, J. Breczko, M. E. Plonska-Brzezinska, A. Z. Wilczewska and L. Echegoyen, *ChemPhysChem*, 2013, **14**, 96–100.
30 Y. V. Butenko, S. Krishnamurthy, A. K. Chakraborty, V. L. Kuznetsov, V. R. Dhanak, M. R. C. Hunt and L. Šiller, *Phys. Rev. B:Condens. Matter Mater. Phys.*, 2005, **71**, 075420.
31 J. Luszczyn, M. E. Plonska-Brzezinska, A. Palkar, A. T. Dubis, A. Simionescu, D. T. Simionescu, B. Kalska-Szostko, K. Winkler and L. Echegoyen, *Chem. – Eur. J.*, 2010, **16**, 4870–4880.
32 T. Pichler, M. Knupfer, M. S. Golden, J. Fink and T. Cabioc'h, *Phys. Rev. B:Condens. Matter Mater. Phys.*, 2001, **63**, 155415.
33 L. Ji, M. Rao, S. Aloni, L. Wang, E. J. Cairns and Y. Zhang, *Energy Environ. Sci.*, 2011, **4**, 5053.
34 G. Siemiaszko, J. Breczko, A. Hryniewicka, A. Ilnicka, K. H. Markiewicz, A. P. Terzyk and M. E. Plonska-Brzezinska, *Sci. Rep.*, 2023, **13**, 6606.
35 G. Siemiaszko, A. Hryniewicka, J. Breczko, K. Brzezinski and M. E. Plonska-Brzezinska, *Chem. Commun.*, 2022, **58**, 6829–6832.
36 G. Siemiaszko, A. Hryniewicka, J. Breczko, O. F. Delgado, K. H. Markiewicz, L. Echegoyen and M. E. Plonska-Brzezinska, *ACS Appl. Polym. Mater.*, 2022, **4**, 2442–2458.
37 A. Hryniewicka, J. Breczko, G. Siemiaszko, A. N. Papathanassiou, K. Góra-Marek, K. A. Tarach, K. Brzezinski, A. Ilnicka, A. P. Terzyk, K. H. Markiewicz, L. Echegoyen and M. E. Plonska-Brzezinska, *Sci. Rep.*, 2023, **13**, 10737.

38 A. Hryniewicka, J. Breczko, G. Siemiaszko, K. Brzezinski, A. Ilnicka, A. P. Terzyk and M. E. Plonska-Brzezinska, *Mater. Adv.*, 2024, **5**, 1065–1077.
39 M. E. Plonska-Brzezinska, *ChemNanoMat*, 2019, **5**, 568–580.
40 S. Xin, L. Gu, N.-H. Zhao, Y.-X. Yin, L.-J. Zhou, Y.-G. Guo and L.-J. Wan, *J. Am. Chem. Soc.*, 2012, **134**, 18510–18513.
41 D. Xu, S. Xin, Y. You, Y. Li, H. Cong and S. Yu, *ChemNanoMat*, 2016, **2**, 712–718.
42 F. Yu, Y. Li, M. Jia, T. Nan, H. Zhang, S. Zhao and Q. Shen, *J. Alloys Compd.*, 2017, **709**, 677–685.
43 Y.-Q. Wang, Y.-S. Zhao, X.-X. Yang, M.-X. Ren, B.-Y. Lei, W.-J. Meng and D.-L. Zhao, *Int. J. Hydrogen Energy*, 2020, **45**, 32654–32663.
44 Z. Wang, J. Cheng, H. Song, D. Xue, X. Zhong and J. Wang, *Energy Technol.*, 2019, **7**, 1900470.
45 W. Zhang, Y. Wang and C. Sun, *J. Polym. Res.*, 2007, **14**, 467–474.
46 P. Bajaj, D. K. Paliwal and A. K. Gupta, *J. Appl. Polym. Sci.*, 1993, **49**, 823–833.
47 X. S. Gai, B. A. Coutifaris, S. H. Brewer and E. E. Fenlon, *Phys. Chem. Chem. Phys.*, 2011, **13**, 5926.
48 S. Arbab and A. Zeinolebadi, *Polym. Degrad. Stab.*, 2013, **98**, 2537–2545.
49 N. A. Kumar, H. Nolan, N. McEvoy, E. Rezvani, R. L. Doyle, M. E. G. Lyons and G. S. Duesberg, *J. Mater. Chem. A*, 2013, **1**, 4431–4435.
50 A. M. Raj and G. C. Thomas, *Sci. Rep.*, 2018, **8**, 13891.
51 A. H. Labulo, B. Omondi and V. O. Nyamori, *SN Appl. Sci.*, 2019, **1**, 142.
52 D. Long, L. Wang, H. Cai, X. Rao and Y. Zhang, *Catal. Lett.*, 2020, **150**, 2487–2496.
53 Y. Wang, D. C. Alsmeyer and R. L. McCreery, *Chem. Mater.*, 1990, **2**, 557–563.
54 M. E. Plonska-Brzezinska, A. T. Dubis, A. Lapinski, A. Villalta-Cerdas and L. Echegoyen, *ChemPhysChem*, 2011, **12**, 2659–2668.
55 D. M. Bobrowska, H. Zubyk, E. Regulska, E. Romero, L. Echegoyen and M. E. Plonska-Brzezinska, *Nanoscale Adv.*, 2019, **1**, 3164–3176.
56 M. Koinuma, H. Tateishi, K. Hatakeyama, S. Miyamoto, C. Ogata, A. Funatsu, T. Taniguchi and Y. Matsumoto, *Chem. Lett.*, 2013, **42**, 924–926.
57 A. Barinov, O. B. Malcioğlu, S. Fabris, T. Sun, L. Gregoratti, M. Dalmiglio and M. Kiskinova, *J. Phys. Chem. C*, 2009, **113**, 9009–9013.
58 D. Hulicova-Jurcakova, M. Seredych, G. Q. Lu and T. J. Bandosz, *Adv. Funct. Mater.*, 2009, **19**, 438–447.
59 J. M. Exley, T. N. Hunter, T. Pugh and M. R. Tillotson, *Powder Technol.*, 2023, **421**, 118387.
60 L. Torrisi, L. Silipigni, M. Cutroneo and A. Torrisi, *Vacuum*, 2020, **173**, 109175.
61 Y. J. Oh, J. J. Yoo, Y. I. Kim, J. K. Yoon, H. N. Yoon, J.-H. Kim and S. B. Park, *Electrochim. Acta*, 2014, **116**, 118–128.
62 Z. Li, Y. Jiang, L. Yuan, Z. Yi, C. Wu, Y. Liu, P. Strasser and Y. Huang, *ACS Nano*, 2014, **8**, 9295–9303.
63 H. Du, X. Gui, R. Yang, Z. Lin, B. Liang, W. Chen, Y. Zheng, H. Zhu and J. Chen, *Nanoscale*, 2018, **10**, 3877–3883.
64 Z. Zhou, T. Liu, A. U. Khan and G. Liu, *Mol. Syst. Des. Eng.*, 2020, **5**, 153–165.
65 K. Yan, L.-B. Kong, Y.-H. Dai, M. Shi, K.-W. Shen, B. Hu, Y.-C. Luo and L. Kang, *J. Mater. Chem. A*, 2015, **3**, 22781–22793.
66 K. S. W. Sing, *Pure Appl. Chem.*, 1985, **57**, 603–619.
67 M. Thommes, K. Kaneko, A. V. Neimark, J. P. Olivier, F. Rodriguez-Reinoso, J. Rouquerol and K. S. W. Sing, *Pure Appl. Chem.*, 2015, **87**, 1051–1069.
68 A. Swiderska-Mocek and E. Rudnicka, *J. Power Sources*, 2015, **273**, 162–167.
69 X. Qiu, Q. Hua, L. Zheng and Z. Dai, *RSC Adv.*, 2020, **10**, 5283–5293.
70 Z. Deng, Z. Zhang, Y. Lai, J. Liu, J. Li and Y. Liu, *J. Electrochem. Soc.*, 2013, **160**, A553–A558.
71 V. L. Kuznetsov, A. L. Chuvilin, Y. V. Butenko, I. Y. Mal'kov and V. M. Titov, *Chem. Phys. Lett.*, 1994, **222**, 343–348.
72 O. Mykhailiv, H. Zubyk, K. Brzezinski, M. Gras, G. Lota, M. Gniadek, E. Romero, L. Echegoyen and M. E. Plonska-Brzezinska, *ChemNanoMat*, 2017, **3**, 583–590.